Research Square

Preprints are preliminary reports that have not undergone peer review.
They should not be considered conclusive, used to inform clinical practice,
or referenced by the media as validated information.

Converged moisture, not vapor transport, governs western United States mountain snowpack

Gerald G. Mace

jay.mace@utah.edu

University of Utah

Article

Keywords: mountain snowpack predictability, moisture-flux convergence, sea-surface-temperature teleconnections, precipitation phase, Upper Colorado River Basin

Posted Date: November 20th, 2026

DOI: https://doi.org/10.21203/rs.3.rs-11599787/v1

License: This work is licensed under a Creative Commons Attribution 4.0 International License.
Read Full License

Additional Declarations: No competing interests reported.

Converged moisture, not vapor transport, governs western United States mountain snowpack

Gerald G. Mace, Department of Atmospheric Sciences, University of Utah, Salt Lake City, UT, USA.

Corresponding author: Gerald G. Mace, Department of Atmospheric Sciences, University of Utah, Salt Lake City, UT 84112, USA. Email: jay.mace@utah.edu

Keywords: mountain snowpack predictability, moisture-flux convergence, sea-surface-temperature teleconnections, precipitation phase, Upper Colorado River Basin

Abstract

A mountain range accumulates snow in proportion not to the water vapor transported past it but to how much is converged over it and falls frozen. Using a budget-derived seasonal moisture supply, $P_b = -\nabla\cdot Q + E$, over seven western United States ranges, we show that once a daily surface-temperature filter separates snow from rain, this frozen convergence tracks basin peak snow water equivalent at r ≈ 0.69–0.92 — far outpredicting the integrated vapor transport emphasized in the atmospheric-river literature (mean r ≈ 0.26). The ocean state's modulation of the converged supply sets the geography of predictability: the northern and coastal ranges' supply is reconstructable out of sample from the concurrent sea-surface-temperature state — ENSO and an Atlantic "Quadpole" mode acting through a North Pacific cyclonic anomaly (cross-validated r ≈ 0.4–0.6) — whereas the Colorado-headwater interior is governed by a regional circulation the leading ocean modes do not reach.

Introduction

Most of the western United States' surface-water supply is stored each winter as mountain snowpack, and its year-to-year variability drives reservoir operations, agriculture, and

drought response (1, 2); as warming shifts the rain–snow line (3, 4), anticipating the coming winter's snowpack before it accumulates is increasingly valuable and necessary. What has been missing is a physical account of what governs how much snow a range accumulates in a given winter — and therefore of where that snowpack can be anticipated a season ahead. Here we show that the governing quantity is neither total precipitation nor the integrated vapor transport emphasized in the atmospheric-river literature (14–18), but the seasonal convergence of moisture over a range and the fraction of it that falls as snow; and that the ocean state's modulation of this converged supply sets the geography of where western snowpack is seasonally predictable.

Several strands of the literature bear on this. The imprint of the El Niño–Southern Oscillation (ENSO) on western snowpack — a wet Southwest and dry Pacific Northwest in warm events, and the reverse in cold — is long established (5–7), and dynamical coupled models skillfully predict western snowpack up to eight months ahead, outperforming observation-based statistics (8). Recently, Stone et al. (21) showed that western United States hydroclimate is governed jointly by ENSO and an Atlantic "Quadpole" sea-surface-temperature mode acting through a North Pacific circulation anomaly, and connected this coupling to drought variability. The interior mountain ranges that supply the Colorado River (hereafter the Upper Colorado River Basin, UCRB; Fig. 1) lie on the node of the ENSO precipitation dipole (9), where the teleconnection changes sign and ENSO explains little of their variance, and internal atmospheric variability has been identified as a fundamental limit on seasonal precipitation predictability (10, 11).

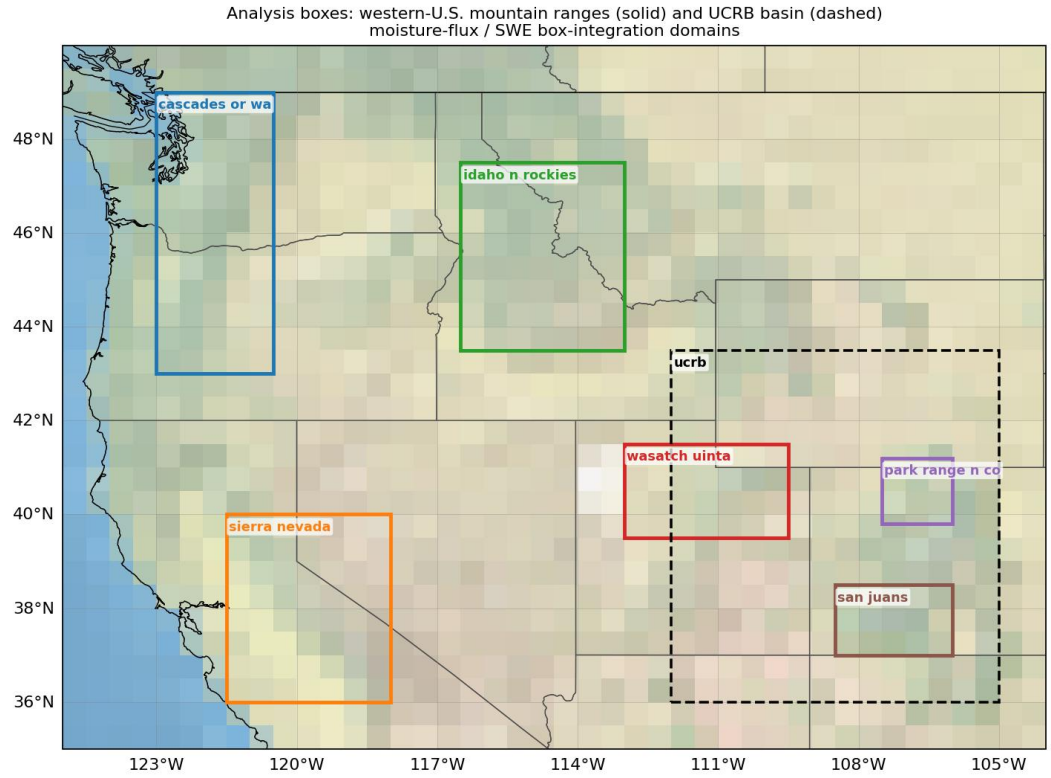


Figure 1. The study domain: the seven range-enclosing boxes over the western United States — six mountain ranges (Cascades, Sierra Nevada, Idaho/Northern Rockies, Wasatch–Uinta, Park Range, San Juans) and the Upper Colorado River Basin (UCRB) — for which the moisture supply P_b and basin peak snow water equivalent are computed.

What remains to be fully resolved is the physical underpinning of this predictability. To address this, we consider three questions: (1) what physically appropriate quantity links the large-scale atmosphere to basin snow water equivalent (SWE); (2) how the sea-surface-temperature modulation of that quantity is distributed geographically; and (3) where seasonal magnitude predictability appears out of reach, what useful characterization of future snowpack, if any, remains.

We approach this through a physically based, budget-derived intermediary. For six western ranges and the UCRB (Fig. 1) we compute the seasonally integrated (October–March), box-averaged, budget-derived moisture supply P_b from ERA5 reanalysis (12). By the atmospheric water-vapor budget, $P_b = -\nabla\cdot Q + E$, where Q is the vertically integrated water-vapor flux (the integrated vapor transport, IVT), E is the surface evaporation, and the small seasonal storage term is neglected (13). P_b is thus the budget-derived seasonal moisture

supply; its evaporation term is a sizeable but nearly constant fraction of the seasonal mean (largest in the dry interior), so the interannual variability that we predict is carried almost entirely by the moisture-flux convergence $-\nabla\cdot Q$ (Materials and Methods). Two properties recommend P_b over precipitation as the target: it is a large-scale, dynamically determined quantity rather than a mixture of the large-scale supply with unresolved orographic and convective processes; and, central to our framing, a mountain range accumulates snow in proportion not to how much vapor is transported past it — the event-scale quantity emphasized in the atmospheric-river literature (14–18) — but, at the seasonal scale, to how much is converged over it. The predictable variability of P_b is therefore that of the seasonal moisture-flux convergence, $-\nabla\cdot Q$.

The prediction then separates into two steps. The conversion of P_b into basin peak SWE is strong once surface temperature is used to separate the supply into rain and snow —the step that makes the prediction of seasonal snowpack of the maritime ranges tractable. The modulation of P_b by the slowly varying SST state is the geographic bottleneck: for the northern and coastal ranges the supply is reconstructable out of sample, confirming and extending the ENSO–Quadpole control of ref. 21 to the moisture supply, whereas the Colorado-headwater interior is not reconstructable from the leading SST modes and the seasonal snowfall is produced by a cyclonic anomaly that is internally forced. For the interior, only a marginal decadal wet/dry odds shift, associated with the Atlantic Multidecadal Oscillation phase, remains.

Results

The moisture supply governs basin snowpack

We first establish that P_b, once converted to snow versus rain, strongly correlates with basin snowpack. Correlating box-integrated P_b with basin peak snow water equivalent from a satellite-era snow reanalysis (19) in the geographic domains of Fig. 1, over 37 winters, gives $r \approx 0.64–0.90$ for six of the seven ranges (Fig. 2); the maritime Cascades ($r = 0.44$) is the clear exception, where a large and variable fraction of the season's precipitation falls as rain or melts, so the total supply does not determine snowpack. That the convergence of vapor, and not its transport, is what governs snowpack is shown directly in Fig. 2: the seasonal magnitude of the vapor transport itself, $|IVT|$, correlates with basin peak SWE only weakly ($r \approx 0.0–0.6$, mean 0.26 across the seven ranges), against $r \approx 0.44–0.90$ for the moisture

supply P_b. Seasonal snow accumulation tracks how much vapor is converged over a range far more closely than how much is transported past it. Filtered gauge precipitation reconstructs peak SWE about as well as the filtered supply in every range, so P_b earns its place as a physically defined, budget-derived quantity that is better observationally constrained than model precipitation and that registers the Atlantic Quadpole more strongly (r = 0.67 vs 0.54 for gauge precipitation; see below).

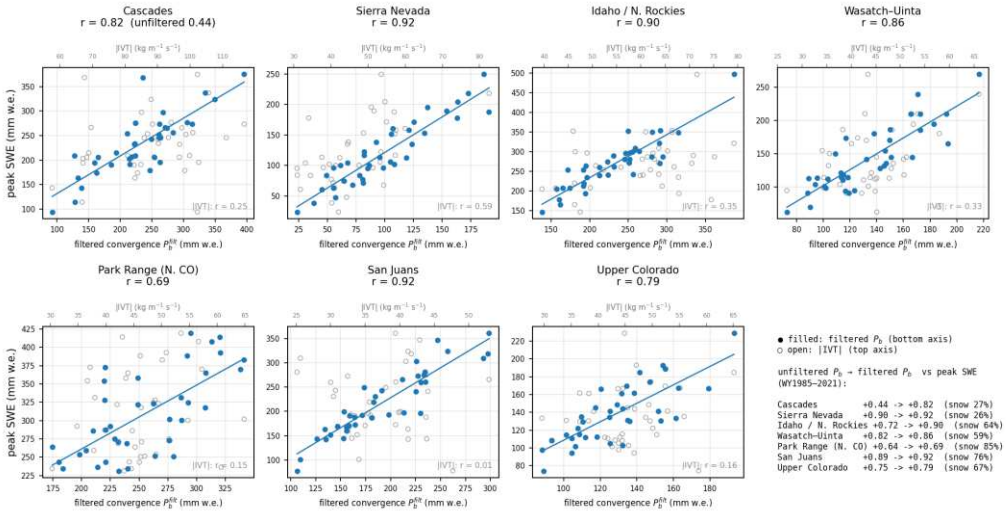


Figure 2. From moisture supply P_b to basin snowpack, temperature-filtered. Filled symbols with least-squares fit (bottom axis): the seasonal frozen moisture supply P_b^{filt} versus basin peak snow water equivalent, all seven ranges (water years 1985–2021). Open symbols (top axis): the seasonal vapor-transport magnitude |IVT| against the same peak SWE. Per-panel correlations are listed (|IVT| at lower right).

From daily reanalysis 2-m temperature and precipitation we compute the season's snow fraction — the precipitation-weighted mean of a daily all-rain-to-all-snow snow-fraction ramp (thresholds from the observed rain–snow temperature distribution, 20) — and scale the seasonal supply by it to obtain a frozen supply, $P_b$filt (Materials and Methods). Against peak snow water equivalent this recovers the Cascades from r = 0.44 to r = 0.82, and improves or holds every other range (Fig. 2); the season's snow fraction, diagnosed independently, ranges from ≈ 0.26 in the warm-maritime ranges (Sierra, Cascades) to 0.6–0.85 in the colder interior ranges — the maritime-to-interior ordering that the mechanism predicts. Because the snow reanalysis itself partitions precipitation phase with a temperature-dependent snow model, we confirmed the recovery against raw SNOTEL peak

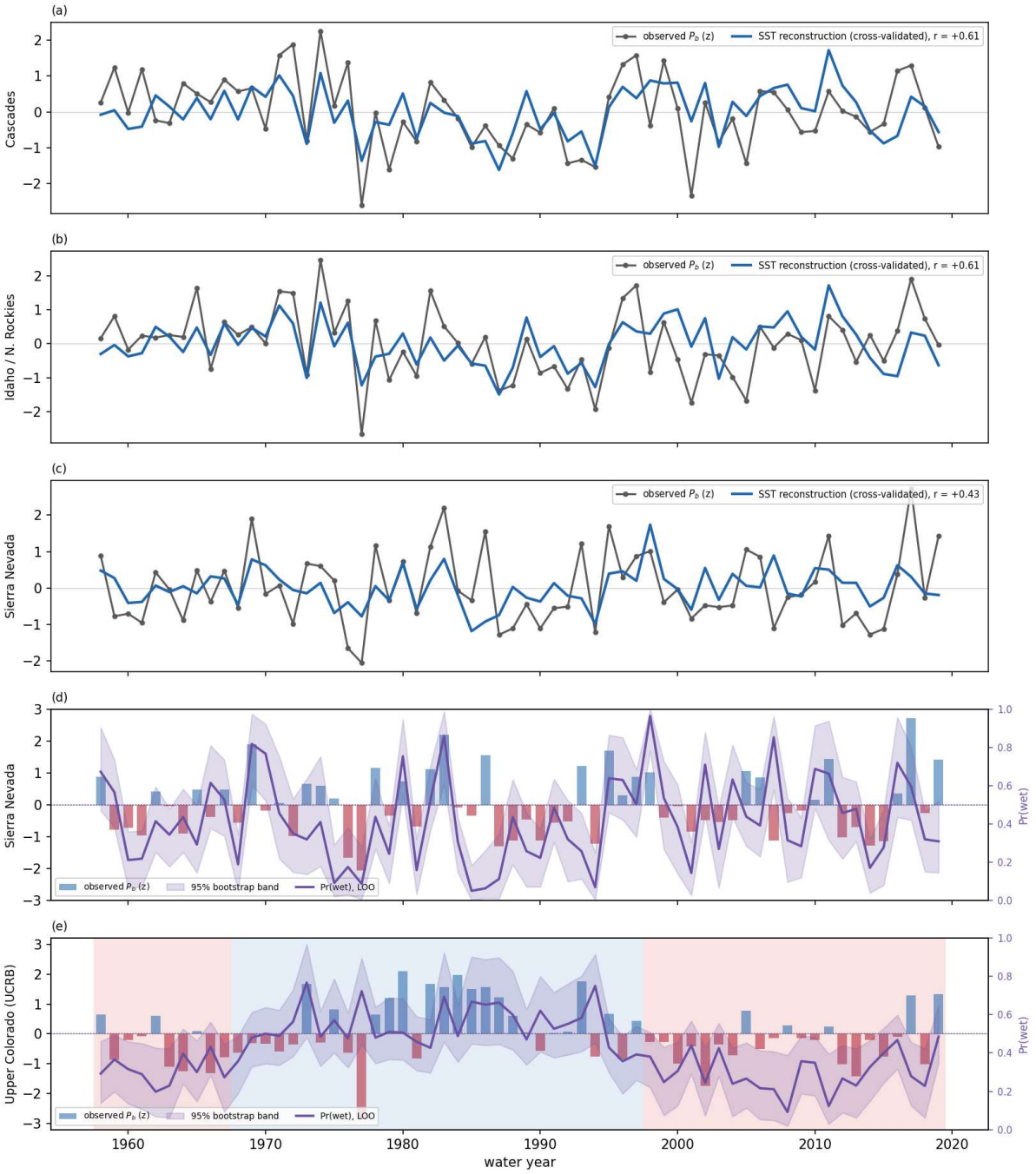
SWE — a direct in-situ measurement with no snow model (4): for the maritime Cascades the filter raises the correlation from r = 0.57 [0.31, 0.76] to 0.92 [0.86, 0.96] (values in brackets are 95% confidence intervals on the correlation, from the Fisher z-transform over the 37 winters; the box index averages 88 SNOTEL stations), matching and exceeding the reanalysis gain, whereas the cold, snow-dominated interior (UCRB) is essentially unchanged (0.69 to 0.64). This recovery is insensitive to how the SNOTEL peak is defined — end-of-month, true daily maximum, or the operational 1-April value — and to holding the station network fixed across the record, ruling out the coarse monthly sampling and the network's growth as artifacts (Supplementary Information, SM3). The filter's construction and thresholds are given in Materials and Methods. With the conversion thus accounted for, we now address the range-specific predictability of P_b.

P_b and the meridional predictability gradient

The seasonal moisture supply P_b inherits predictability from the slowly varying state of the global ocean as represented by SST. P_b is a function of the time-varying synoptic state; the occurrence frequency of the circulations that converge moisture is ultimately influenced by how the ocean state conditions the placement and intensity of the planetary-scale atmospheric circulation. This is a teleconnection — a chain of causality that is often neither direct nor well understood. We adopt the shorthand that the ocean state modulates P_b, with the teleconnection understanding assumed throughout. Reproducing the coupled SST modes from the Hadley Centre SST product (Materials and Methods), the leading predictors of the western supply are ENSO and an Atlantic "Quadpole" (21) — a north–south Atlantic SST mode that couples to P_b more strongly ($r \approx 0.67$) than it does to GPCC gauge precipitation (0.54). These modes modulate the P_b of the coastal and northern ranges through a standing North Pacific cyclonic anomaly shown in ref. 21 (their fig. 2): this trough is the proximate circulation that the SST state influences, and it is a mechanism by which an Atlantic SST anomaly can modulate precipitation over western North America (ref. 21 emphasizes in addition a tropical-Atlantic/ITCZ pathway for the Quadpole). The two modes combine additively on the supply — an ENSO×Quadpole interaction (the difference-in-differences of the tercile-phase composite) is not statistically significant in any range (permutation $p \geq 0.14$) — so an additive predictor set is retained. The interior ranges that form the upper Colorado River headwaters (UCRB) are not reached individually or collectively by this pathway; ref. 21 reports an Atlantic-Quadpole influence extending into the Colorado headwaters, a transition zone (9) where the western precipitation dipole

changes sign. Our out-of-sample result sharpens that picture: we reproduce ref. 21's in-sample Atlantic-Quadpole footprint over the interior ($|r| \approx 0.2–0.34$), but it does not survive leave-one-out cross-validation ($r_{CV} \approx 0$) — the in-sample footprint is confirmed, the out-of-sample skill is absent — locating where the ocean modulation appears not to reach.

In a leave-one-winter-out reconstruction, the concurrent winter (October–March) SST state accounts for northern and coast-range P_b out of sample at $r \approx 0.6$ (Cascades, Idaho) but for essentially none of the interior's (Fig. 3). This is a *concurrent* diagnosis — the SST modes and P_b describe the same season — of how much of the supply the ocean state accounts for, not a forecast. This northern skill derives mainly from the Atlantic Quadpole; because that mode is derived from the full record, we bound any pattern-derivation leakage with strictly independent, externally defined indices (Niño-3.4 and an Atlantic SST index that never see the supply or the analysis precipitation), which reconstruct the same northern P_b at $r \approx 0.36–0.44$ — a fully external, leakage-free reconstruction (conservative: the external Atlantic index is the AMO, not the Quadpole, so this does not by itself validate the Quadpole attribution or constitute a guaranteed lower bound), against the $r \approx 0.6$ full-record value (Materials and Methods). The Sierra's magnitude has no external-index skill (its external reconstruction is ≈ 0). The gradient is geographically sharp: the interior boxes lie on the node of the Atlantic Quadpole's response, where its influence changes sign, and no SST pattern that we investigated reconstructs the P_b of the UCRB or any of the interior ranges that compose it. Predictability of the P_b magnitude thus appears to be a northern and coastal-range property of the mountain ranges considered (Fig. 1).



170

171 **Figure 3.** Cross-validated SST (ENSO + Atlantic Quadpole) reconstruction of winter P_b and
172 the wet/dry sign, 1958–2019. (a–c) Magnitude: observed P_b (grey) versus the leave-one-out
173 SST reconstruction (blue) for (a) the Cascades, (b) Idaho/N. Rockies, and (c) the Sierra
174 Nevada. (d) The Sierra wet/dry sign: observed anomaly (bars, blue wet / red dry, left axis)
175 with the leave-one-out reconstruction as a calibrated probability Pr(wet) (purple line, right
176 axis; dotted at ½) and its 95% winter-resampling bootstrap band. (e) The UCRB counter-

example, with the sign reconstructed from the AMO: same Pr(wet) line and band, and the AMO decadal phase as background (pink warm → dry, blue cool → wet).

A pointwise regression of each range's supply on the seasonal 500-hPa height field shows that the interior ranges that form the UCRB respond to a local cyclonic anomaly located over or just west of the UCRB — a Great-Basin/Four-Corners feature — with which the interior P_b correlates concurrently at $|r| \approx 0.55$ (a linear correlation, not a variance fraction; Fig. 4). This cyclonic anomaly is regional in that its magnitude is not recoverable from the leading SST modes (the best any pattern achieves, cross-validated, is ≈ 0.2, and the strongest single predictor — decadal only — is the Atlantic Multidecadal Oscillation), land-surface persistence via soil moisture of the prior season is null, and it projects onto the higher-order regional circulation modes that are orthogonal to the large-scale ocean teleconnections. The interior's controlling degree of freedom is therefore regional atmospheric variability that is unreconstructed by the leading SST modes — consistent with stationary-wave theory (22) and the internal variability of the eddy-driven jet (23). This is consistent with the internal-variability limit invoked generically in prior work (10, 11). We frame it as an absence of skill from the leading SST modes over this record rather than proof that no ocean state modulates the interior via teleconnections. Four additional geophysical phenomena were found to have no relationship to the variability of the interior cyclonic anomaly. These include: ENSO "flavor" (Niño-3, Niño-4, and the Modoki index), being nearly collinear with the ENSO mode, does not improve the cross-validated interior reconstruction when added to it; the seasonal stratospheric polar vortex (10-hPa zonal-mean zonal wind at 60°N) gives no out-of-sample increment either, only a weak, non-significant residual association (interior-residual correlation ≤ +0.2); seasonal tropical convection (ERA5 outgoing longwave radiation) shows no coherent significant center over the interior residual — the fraction of significant cells is at the ∼5 % false-positive rate; and the subseasonal Madden–Julian Oscillation, composited by phase, leaves interior precipitation essentially unmodulated (daily composite range 0.01–0.04 mm day^{-1} across the eight phases, with no dependence on the AMO phase). The signal-to-noise paradox (24) nonetheless cautions that a weak forced signal can be under-detected, so these are bounds on, not disproof of, a residual forced signal. Consistent with this caution, an autumn quasi-biennial-oscillation precursor of southwestern-U.S. (including interior) winter precipitation has recently been documented (37) — a stratospheric lead pathway complementary to the concurrent analysis here.

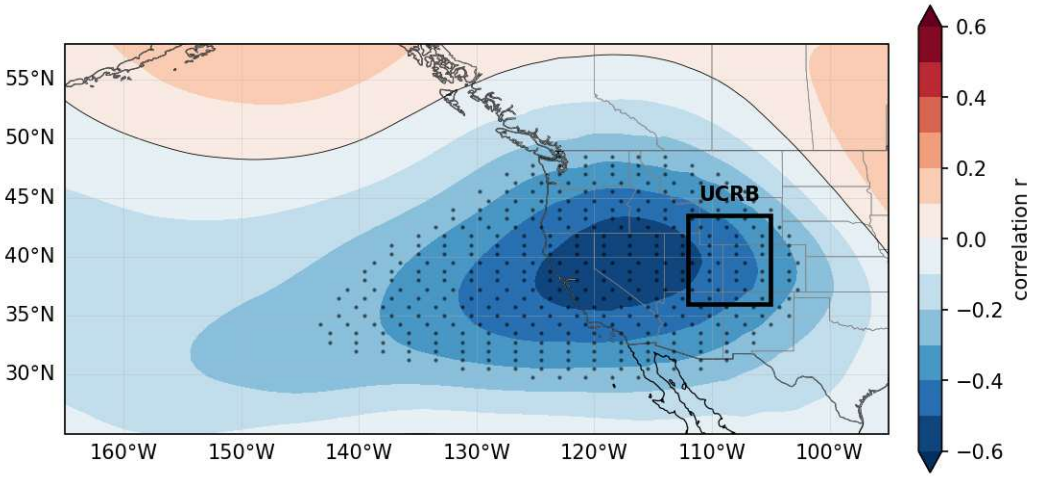


Figure 4. Correlation of the UCRB winter moisture supply P_b with the seasonal 500-hPa height field. A local cyclonic anomaly (blue, low heights) sits over the Great-Basin/Four-Corners just west of the UCRB (a concurrent regression, not a demonstrated forcing). Stippling marks $p < 0.05$ (two-tailed t-test with effective degrees of freedom, ref. 31).

Because the UCRB ranges' P_b magnitude is unreconstructed by the leading SST modes, its seasonal magnitude is not recoverable from the ocean SST state. Its wet/dry sign, however, does carry a weaker, decadal signal, which we report as a diagnostic association. Scored by the ranked probability skill score (RPSS; the fractional reduction in probabilistic error relative to a climatological forecast, 0 for no skill and 1 for perfect, 25), a wet/dry-tercile reconstruction is genuinely skillful in the north (Cascades RPSS = 0.30, fold-contained, 5000-sample winter-bootstrap 95 % CI [0.14, 0.45], excluding zero; substantial by the standards of seasonal winter precipitation, whose predictability is limited, 10, 11) but only marginally positive in the Upper Colorado (RPSS = 0.09 [−0.04, 0.21], spanning zero). The interior signal is best read as a decadal wet/dry odds shift, not a per-winter result: the Upper Colorado's sign matches the concurrent AMO phase in 69 % of winters against a 58 % climatological majority, but a rule that simply sets "wet when the low-pass Atlantic Multidecadal Oscillation is cool" reproduces that same 69 % (67 % under a strictly causal, trailing low-pass), so the fitted logistic adds nothing over the raw AMO phase. Against a serial-correlation-preserving surrogate that respects the AMO's decadal persistence (Materials and Methods) the association is only marginally significant ($p \approx 0.035$), and the UCRB is the one interior unit that reaches even that level — the sub-basins that compose it are individually at chance (Wasatch–Uinta 56 %, Park Range 60 %, San Juans 58 %; none

significant), so the result does not survive a family-wise correction across the interior ranges. It is nonetheless stable out of sample, holding under leave-block-out (66 %) and forward rolling-origin (70 %) validation, both above the 58 % majority. The seasonal odds shift here and the decadal AMO correlation developed in the Discussion are two views of one low-frequency relationship and not independent evidence. Figure 3e shows the AMO decadal phase against the winter-by-winter outcomes: the interior product is which AMO phase the coming winters occupy rather than a seasonal forecast.

Cast as calibrated probabilities, the same diagnosis assigns each winter a Pr(wet) with a 95 % interval (Supplementary Fig. S2; Materials and Methods). Where the sign is SST-modulated these are well-calibrated and genuinely per-winter — for the Sierra the reliability diagram follows the diagonal (Brier skill score +0.14) and for the northern ranges +0.20 to +0.24 — whereas for the interior they are only marginally skillful (UCRB +0.05, indistinguishable from zero) and largely trace the AMO decadal envelope rather than resolving individual winters, with the interior sub-basins at climatology.

The Sierra Nevada is an instructive intermediate case (Fig. 3c,d). Its P_b magnitude is only weakly reconstructed ($r \approx 0.43$, versus ≈ 0.61 for the Cascades and Idaho) for two reasons: it lies near the node of the ENSO precipitation dipole — its ENSO correlation is weak and of opposite sign to the northern ranges ($r \approx +0.2$, wetter in El Niño, versus drier in the north), so the ENSO term contributes little — leaving the Atlantic Quadpole as its only effective oceanic modulation ($r \approx 0.44$); and its seasonal accumulation is dominated by a small number of atmospheric-river events whose seasonal number and landfall latitude are largely synoptic, adding internal variance to the seasonal magnitude. Its wet/dry sign, however, tracks the SST state (Fig. 3d): the sign of the Sierra anomaly matches the concurrent Quadpole in 69 % of winters ($p = 0.002$), comparable to the northern ranges. The Sierra thus resembles the interior in that only its sign is reliably recoverable, but the mechanism differs — the Sierra's sign is SST-modulated through the Quadpole, whereas the interior's appears to follow only the decadal Atlantic Multidecadal Oscillation (Fig. 3e).

The 2025–26 winter as a diagnostic illustration

The 2025–26 winter, during which historically low snowfall occurred through the interior of the UCRB, illustrates these concepts. This is a diagnostic, post-hoc decomposition rather than an independent forecast test. With that caveat, the winter's weak-La-Niña pattern appears to have contributed to a P_b between 1 and 2 σ below the mean but an

approximately normal north. The AMO decadal phase correctly anticipated the dry interior. The winter was also historically warm, +2 σ (Cascades) to +4 σ (UCRB); in the maritime north — chiefly the Cascades, whose accumulation straddles the rain–snow line — much of the adequate supply fell as rain or melted whereas the colder continental ranges such as Idaho stayed snow-dominated despite the warmth. Diagnostically, the temperature filter attributes that maritime low-snow year to a reduced snow fraction rather than a significant moisture deficit, whereas the interior low-snow was a genuine P_b deficit. These are not fully independent causes: dynamically, a persistent ridge produces both subsidence/moisture divergence (low P_b) and warmth (rain rather than snow), so the decomposition separates the two effects on snowpack diagnostically and not as independent forcings. What the 2025–26 shows is that low snowpack across the West arose from two distinguishable but not entirely independent mechanisms — an interior moisture-supply deficit and a temperature-driven conversion loss in the maritime north.

Discussion

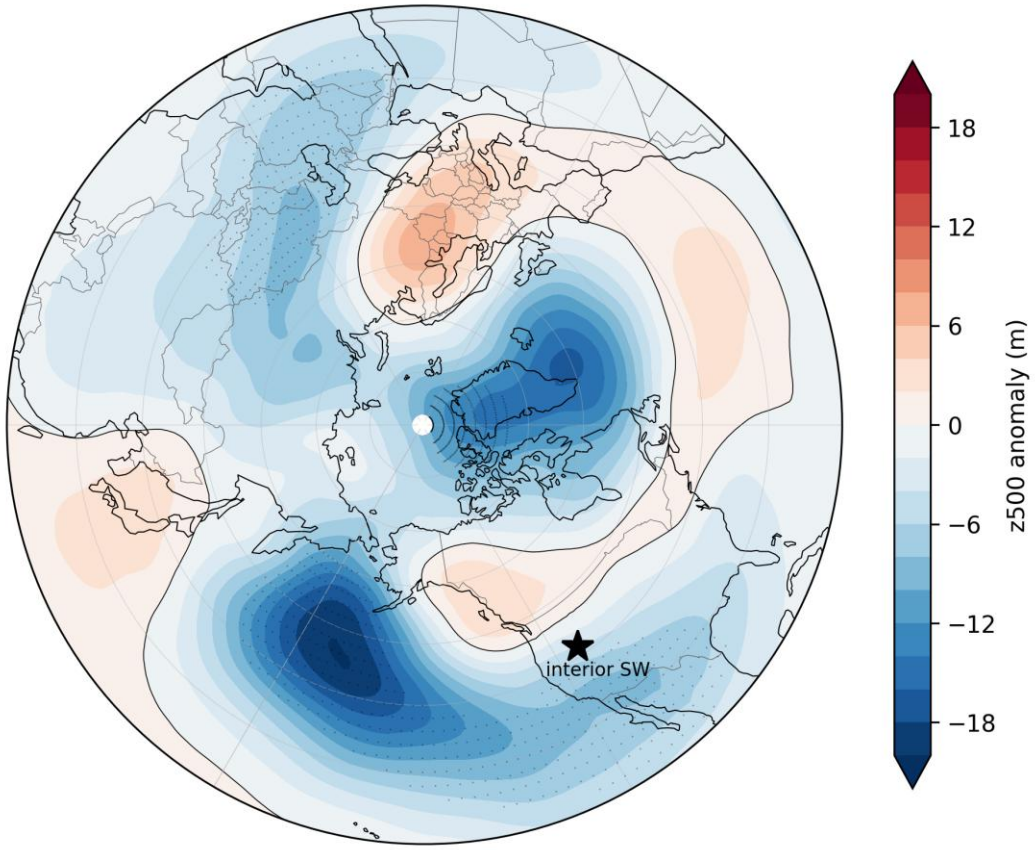
What governs a mountain range's snowpack is the snow fraction of the moisture converged over it, not the vapor transported past it; and the ocean's modulation of that converged supply — rather than of precipitation — divides the geography of where that snowpack is predictable. The northern and coastal ranges' P_b has a substantial externally modulated component – ENSO and the Atlantic Quadpole acting through a North Pacific cyclonic anomaly – so a large fraction of their moisture supply is explainable from the concurrent ocean state, which itself persists from the preceding autumn. On the other hand, the slowly varying SST modes do not appear to influence the P_b of the interior UCRB where its snowfall appears consistent with the internal variance of the extratropical seasonal mean (10, 11). Where the magnitude is out of reach, however, the interior retains a marginal decadal wet/dry association with the AMO phase that appears more as a decadal odds shift.

That this geography of modulation emerges at all hinges on the choice of intermediary. Integrated vapor transport would not resolve it. The interior's controlling anomaly is a convergence feature to which a transport metric is insensitive (consistent with the weak |IVT|–accumulation correspondence of Fig. 2); gauge precipitation, though nearly equivalent to P_b interannually (Methods), convolves the modulated supply with the unmodulated, temperature-controlled conversion and registers the Atlantic Quadpole more

weakly (r = 0.54 vs 0.67). The budget-derived supply is convergence-based yet phase-separated, and so is the only one of the three that isolates the modulated signal and lets the north–interior divide be attributed to ocean modulation rather than to conversion.

These results complement and refine the demonstration that dynamical models can skillfully predict western snowpack (8). Where that work identified the maritime ranges as the difficult case owing to their chaotic character, we show the maritime difficulty to be a rain-versus-snow conversion problem, recoverable from temperature (Fig. 2); what sets the interior apart is instead its local cyclonic anomaly, which the tested SST modes do not reconstruct. Skill in P_b is, moreover, not the same as skill in snowpack under warming: the 2025–26 winter shows the conversion pathway overriding an adequate supply in the northern ranges, a decoupling expected to grow (26, 27).

On multidecadal timescales the interior P_b associated with the regional cyclonic anomaly appears to covary with the Atlantic Multidecadal Oscillation (AMO): a cool North Atlantic accompanies a deepened North Pacific trough that extends southeastward over the interior ranges (Fig. 5), and a warm Atlantic a retracted trough and a drier interior. The covariation is confined to the decadal band (9-year low-pass $r \approx -0.67$; the year-to-year correlation is near zero, Fig. 6), and its sign matches the established warm-AMO/U.S.-drought relationship (refs. 28, 29). The low-passed record affords few effective degrees of freedom, so we treat the coefficient as suggestive rather than definitive: against persistence-aware red-noise surrogates the decadal correlation is marginally significant ($p \approx 0.035$, rising to $\sim$0.06 under a more persistent AMO null; the interior is near-white year-to-year, so the near-white null is the physical one) and its magnitude weakly constrained (a moving-block bootstrap 95 % interval, [−0.85, +0.05], includes zero). The AMO here is an a-priori predictor from the established warm-AMO/U.S.-drought link (28, 29). The physical interpretation therefore rests less on this single marginal coefficient than on its sign consistency with coupled AMV pacemaker experiments (30). So framed, the AMO constrains only the decadal background of interior snowfall.



323

324 **Figure 5.** Hemispheric winter 500-hPa height anomaly regressed on the cool AMO phase
325 (metres per −1 σ AMO; star marks the interior Southwest). Stippling marks $p < 0.05$ (two-
326 tailed t-test, effective degrees of freedom). The decadal-band (9-yr low-pass) companion is
327 Supplementary Fig. S3.

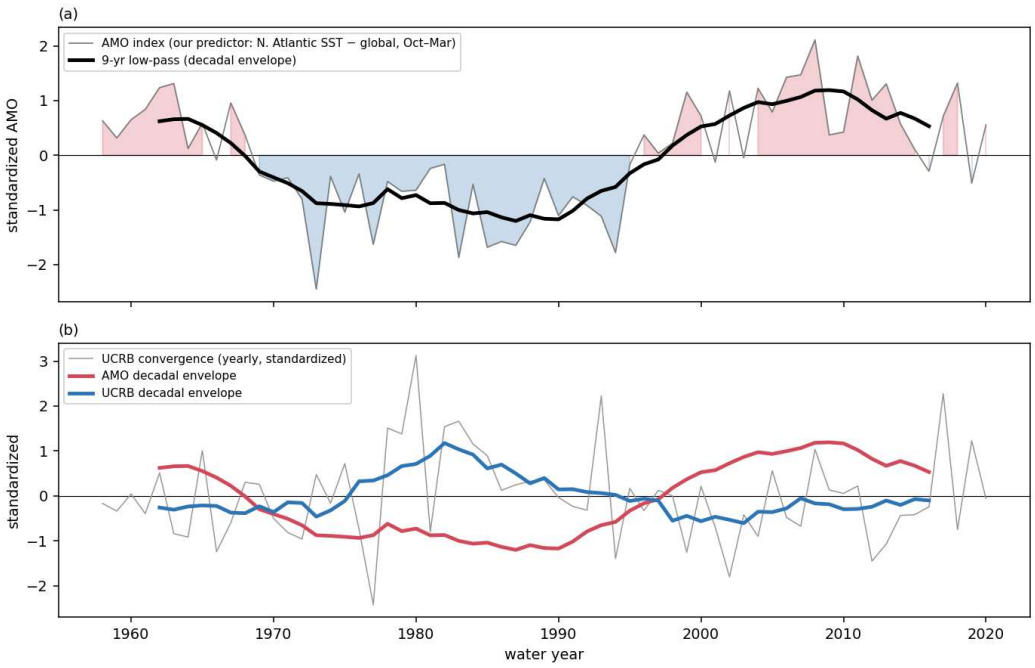


Figure 6. The Atlantic Multidecadal Oscillation index (North Atlantic minus global SST, October–March) with its decadal envelope, shown against the UCRB moisture supply.

Methods

Moisture budget and boxes. Seasonally integrated, box-averaged, budget-derived moisture supply P_b was computed for seven range-enclosing boxes (~150–300 km) from fifth-generation reanalysis (ERA5; 12) monthly fields using the aerological formulation of ref. 13, with evaporation retained and the negligible seasonal storage term dropped; box means are cosine-latitude-weighted and include all box cells (the budget requires the divergent cells). The seven boxes were fixed a priori on physiographic grounds; one — the Park Range — was adjusted once early in the analysis (recentered on the range crest to enclose a single snow regime, on a box-size-stability criterion tied to the Fig. 2 conversion, before the SST-modulation analysis), and the interior predictability results do not depend on it (the Park Range is an interior null range). Across the seven boxes the evaporation term is 17–84 % of the seasonal-mean convergence (smallest in the maritime Cascades, largest in the dry interior), but it contributes negligibly to interannual variability: $-\nabla\cdot Q$ and P_b anomalies correlate at r = 0.98–1.00, and the evaporation anomaly has a standard deviation of only ≈ 8–12 mm, so the predictable year-to-year variability of P_b is that of the convergence. The neglected seasonal storage term is small (the October–March change in

box-mean column water vapor is 0.6–3.0 % of P_b), and the budget closes: P_b tracks ERA5 total precipitation at r = 0.97–0.99, the one-signed 8–18 % deficit (P_b < reanalysis precipitation) being the data-assimilation analysis increment rather than storage or numerical error (Supplementary Information, SM1; `pb_closure.py`). **Snow filter (conversion).** Daily ERA5 2-m temperature and precipitation (October–March, 1984–2021) were used to weight each day's precipitation by a snow fraction fsnow(T), a linear all-rain-to-all-snow ramp between T = +2.5 °C and T = −0.5 °C, a fixed band chosen to bracket the central tendency of the observed — and spatially varying — Northern-Hemisphere rain–snow temperature distribution (20) (a modeling choice; ref. 20 documents that distribution, not this specific ramp); the season's snow fraction is the precipitation-weighted mean of fsnow (a number between 0 and 1), and the filtered supply P_b^{filt} is the seasonal supply P_b multiplied by that snow fraction — i.e., the portion of the season's supplied moisture that fell as snow rather than rain. The snow fraction is a ratio and so is independent of the daily-precipitation rate/total convention. This is a seasonal-scalar treatment: the phase is applied to the season-total supply rather than resolved day by day, so it neglects any within-season covariance between the daily supply and its phase; because the snow fraction is precipitation-weighted, days with more precipitation dominate it, which is the physically relevant weighting for snow accumulation. Because P_b is a coarse box-mean while peak SWE resolves the accumulating snowpack, the Fig. 2 axes are not expected to match 1:1 (peak SWE runs ∼10–20 % above the filtered supply, per-range slope ≈ 1, consistent with ERA5's orographic underestimate; gridded and reanalysis precipitation underestimate cold-season snowfall over the Upper Colorado headwaters by ∼30–65 % against in-situ and airborne-lidar measurements (38–40), while snowpack sublimation — directly measured in the same headwaters at ∼8–10 % of peak snow water equivalent (41, 42) — acts in the opposite sense, so the supply underestimate exceeds the net offset); this near-constant per-range offset is absorbed into the cross-validated regression and does not affect the reported skill. **Predictands.** Basin peak snow water equivalent from the western United States snow reanalysis (19; data set 35, water years 1985–2021), taken as the water-year maximum of the basin-mean SWE (the peak date varies by basin and year) and aggregated over the reanalysis pixels within each range box, so the snow predictand shares the box footprint of the atmospheric P_b but resolves the mountain snowpack at finer scale; the WUS reanalysis is a model–data assimilation of Landsat fractional snow-covered area, not a direct SWE observation, and its posterior uncertainty is not propagated here; because

it partitions precipitation phase with a temperature-dependent snow model, the Fig. 2 recovery was confirmed against model-free raw SNOTEL peak SWE (4; per-station z-scores averaged within each box), which reproduces the maritime gain and the interior's insensitivity and is robust to the peak definition (monthly, daily, or 1-April) and to a fixed station network. Gauge precipitation from PRISM (34) is used for validation; because PRISM underestimates headwater peak snow water equivalent by ~30 % against airborne lidar (39), the model-free SNOTEL cross-check (SM3) is the more reliable anchor for the cold interior. The conversion analysis (Fig. 2) spans the snow-reanalysis period (water years 1985–2021, N = 37); the SST-modulation analysis (Fig. 3; Table S1) uses the longer 1958–2019 window (N = 62) over which the coupled SST modes are defined. **Predictors.** Coupled SST modes from a from-scratch maximum-covariance analysis of HadISST (33) against GPCC gauge precipitation (36; Full Data Reanalysis V2020, 1° monthly, 1891–2019); the Atlantic Multidecadal Oscillation, ENSO indices (Niño-3, Niño-3.4, Niño-4). **Statistical methods.** All predictive skill is evaluated out of sample by leave-one-out cross-validation (32); reported reconstruction correlations are between cross-validated reconstructions and observations, and quantities described as concurrent (the interior circulation ceiling, the height-field regressions) are in-sample covariance diagnostics rather than forecasts. The SST modes are derived from a 128-winter (1892–2019) SST–precipitation maximum-covariance analysis, so leaving out one winter of the 1958–2019 regression window removes one of 128 winters from the mode derivation and shifts the patterns by ≈1%, making mode-derivation leakage second-order; re-standardizing the predictors and predictand within each fold leaves the skill unchanged (Cascades/Idaho cross-validated r 0.61→0.63), and strictly external, MCA-independent indices (Niño-3.4 and an Atlantic SST index computed directly from HadISST, never touching the supply or the analysis precipitation) reconstruct the coastal/northern P_b at r ≈ 0.36–0.44 — a fully external, leakage-free reconstruction (conservative, as the external Atlantic index is the AMO, not the Quadpole; not a guaranteed lower bound) versus r ≈ 0.6 full-record. A fully nested per-fold re-derivation of the modes was not performed (the MCA builder is not archived), so we report both figures rather than a single number. Confidence intervals use the Fisher z-transform; the significance of correlations and of the pointwise height-field regression (Fig. 5) uses a two-tailed t-test with the sample size reduced for serial correlation in both series (ref. 31; effective degrees of freedom $N_e = N(1-a_1b_1)/(1+a_1b_1)$), shown by stippling at $p < 0.05$ (computed pointwise). Decadal and interannual components are separated with a 9-

year centered low-pass filter, decadal correlations interpreted as descriptive of the multidecadal background; because the low-pass leaves few effective degrees of freedom, their significance is assessed against first-order autoregressive [AR(1)] red-noise surrogates filtered identically (rather than by a Fisher interval on the autocorrelated filtered series), and the interior AMO correlation so tested is marginally significant ($p \approx 0.035$, rising to ~0.06 under a redder AMO null). Sign skill is scored against an unbiased climatological expectation; for the SST-modulated (coastal/northern) ranges, whose predictors are near-white year to year, significance uses a one-sided binomial test, whereas for the decadally forced interior (AMO) the binomial is inflated by the predictor's persistence and significance is instead assessed against a circular-shift surrogate null that preserves the AMO's autocorrelation (the AMO series is circularly shifted against the sign series at every non-trivial lag; the p-value is the fraction of shifts whose leave-one-out hit rate matches or exceeds the observed). The interior sign is additionally validated by leave-block-out and forward rolling-origin cross-validation and benchmarked against decadal-phase, sign-persistence, and majority-class baselines (SI). Probabilistic tercile skill uses the ranked probability skill score against a climatological forecast, with reliability diagrams and the Brier score. The coupled SST modes use maximum covariance analysis (SVD of the temporal cross-covariance of detrended, standardized SST and precipitation) over complete winters; the SST-mode coefficients (N, Q) are standardized over the 1892–2019 mode record and the AMO index over the 1958–2019 analysis window (the fitted regression coefficients absorb each predictor's scale, so cross-validated skill is unaffected). Key results are confirmed on linearly detrended series.

Prediction equations. The magnitude is reconstructed by linear regression of the standardized supply on the two standardized SST modes, $\hat{y}_t = \beta_0 + \beta_1 N_t + \beta_2 Q_t$ (N_t = ENSO, Q_t = Quadpole), back-transformed to millimetres as $P_b = \bar{P}_b + \sigma_Pb \cdot \hat{y}$ with the per-range mean and standard deviation. The wet/dry sign is a logistic regression on (N, Q) — on the standardized AMO index for the interior, whose sign is not SST-modulated — with the wet class assigned when the leave-one-out Pr(wet) exceeds ½; each winter's Pr(wet) carries a 95 % interval from the logistic coefficient covariance, confirmed by a winter-resampling bootstrap. The full equations, the r_CV and prediction intervals, the coefficient-covariance derivation, and the per-range fitted coefficients are given in Supplementary Information (SM5, Table S1).

Code and reconstruction tool. Documented Python implementations of the magnitude and sign equations are provided as a citable code deliverable (Supplementary Dataset S1). A runnable script (`apply_reconstruction.py`) returns the standardized predictors — N_t (ENSO) and A_t (AMO) are also available from standard operational indices, while Q_t (the Quadpole) is computed from the SST field — evaluates the equations above, and prints, for a chosen winter and every range, the reconstructed P_b with its 95 % interval and Pr(wet); a worked example (water year 2016) is included.

Use of large language models. A large language model (Claude; Anthropic, Claude Opus 4.8, accessed through the Claude Code interface) assisted with analysis code, literature review, and manuscript preparation. The author conceived and designed the study, directed all analyses, and verified all code, results, figures, and references. The study's hypotheses, interpretations, and conclusions are the author's own. No text, data, or figures were produced for publication without author verification; all figures are data plots generated by the analysis code, and no generative-AI image tools were used. The author is solely responsible for the content.

Data availability. All input data are public: ERA5 (Copernicus Climate Data Store); HadISST (UK Met Office Hadley Centre); PRISM (PRISM Climate Group, Oregon State University); GPCC precipitation (DWD/GPCC, ref. 36); the WUS-SR snow reanalysis (NSIDC, ref. 35); and SNOTEL snow water equivalent (USDA NRCS Air-Water Database REST API).

Code availability. The analysis code — the moisture-budget and box-integration routines, the temperature filter, the maximum-covariance predictor reconstruction, the leave-one-out and blocked/forward cross-validation, the sign-skill surrogate tests, the reproduction equations, and every figure script — is deposited at Zenodo (https://doi.org/10.5281/zenodo.23068639) and released publicly on publication; the reproducible reconstruction tool (apply_reconstruction.py) is included.

Acknowledgements

This work was supported by the National Science Foundation under grant 2348449. I thank colleagues in the Department of Atmospheric Sciences, University of Utah — Court Strong, Thomas Reichler, Alyssa Stansfield, Jim Steenburgh, Gregory Egger, and Gannet Hallar — for valuable discussions of this work, and Anne Lang, whose Master's thesis inspired it. The

analysis code, literature review, and manuscript preparation were assisted by Claude (Anthropic; Claude Opus 4.8, via the Claude Code interface); the author directed the work, verified all code, results, figures, and references, and is solely responsible for the content. The figures are data plots produced by the analysis code; no AI image-generation tools were used.

Author contributions: G.G.M. designed research, performed research, analyzed data, and wrote the paper.

Competing interests: The author declares no competing interests.

Supplementary Figures S1–S3 and Supplementary Table S1 appear in the Supplementary Information.

References

1. Bales, R. C. et al. Mountain hydrology of the western United States. Water Resour. Res. 42, W08432 (2006).
2. Barnett, T. P., Adam, J. C. & Lettenmaier, D. P. Potential impacts of a warming climate on water availability in snow-dominated regions. Nature 438, 303–309 (2005).
3. Mote, P. W., Hamlet, A. F., Clark, M. P. & Lettenmaier, D. P. Declining mountain snowpack in western North America. Bull. Am. Meteorol. Soc. 86, 39–49 (2005).
4. Serreze, M. C., Clark, M. P., Armstrong, R. L., McGinnis, D. A. & Pulwarty, R. S. Characteristics of the western United States snowpack from snowpack telemetry (SNOTEL) data. Water Resour. Res. 35, 2145–2160 (1999).
5. Redmond, K. T. & Koch, R. W. Surface climate and streamflow variability in the western United States and their relationship to large-scale circulation indices. Water Resour. Res. 27, 2381–2399 (1991).
6. Cayan, D. R. Interannual climate variability and snowpack in the western United States. J. Clim. 9, 928–948 (1996).
7. Dettinger, M. D., Cayan, D. R., Diaz, H. F. & Meko, D. M. North–south precipitation patterns in western North America on interannual-to-decadal timescales. J. Clim. 11, 3095–3111 (1998).
8. Kapnick, S. B. et al. Potential for western US seasonal snowpack prediction. Proc. Natl. Acad. Sci. USA 115, 1180–1185 (2018).

9. Wise, E. K. Spatiotemporal variability of the precipitation dipole transition zone in the western United States. Geophys. Res. Lett. 37, L07706 (2010).
10. McKinnon, K. A. & Deser, C. The inherent uncertainty of precipitation variability, trends, and extremes due to internal variability, with implications for Western US water resources. J. Clim. 34, 9605–9622 (2021).
11. Clark, J. P. & Johnson, N. C. Evaluating predictability limits of North American winter precipitation. npj Clim. Atmos. Sci. 8, 254 (2025).
12. Hersbach, H. et al. The ERA5 global reanalysis. Q. J. R. Meteorol. Soc. 146, 1999–2049 (2020).
13. Seager, R. & Henderson, N. Diagnostic computation of moisture budgets in the ERA-Interim reanalysis with reference to analysis of CMIP-archived atmospheric model data. J. Clim. 26, 7876–7901 (2013).
14. Ralph, F. M. et al. Flooding on California's Russian River: role of atmospheric rivers. Geophys. Res. Lett. 33, L13801 (2006).
15. Neiman, P. J., Ralph, F. M., Wick, G. A., Lundquist, J. D. & Dettinger, M. D. Meteorological characteristics and overland precipitation impacts of atmospheric rivers affecting the West Coast of North America based on eight years of SSM/I satellite observations. J. Hydrometeorol. 9, 22–47 (2008).
16. Guan, B., Molotch, N. P., Waliser, D. E., Fetzer, E. J. & Neiman, P. J. Extreme snowfall events linked to atmospheric rivers and surface air temperature via satellite measurements. Geophys. Res. Lett. 37, L20401 (2010).
17. Dettinger, M. D., Ralph, F. M., Das, T., Neiman, P. J. & Cayan, D. R. Atmospheric rivers, floods and the water resources of California. Water 3, 445–478 (2011).
18. Rutz, J. J., Steenburgh, W. J. & Ralph, F. M. Climatological characteristics of atmospheric rivers and their inland penetration over the western United States. Mon. Weather Rev. 142, 905–921 (2014).
19. Fang, Y., Liu, Y. & Margulis, S. A. A western United States snow reanalysis dataset over the Landsat era from water years 1985 to 2021. Sci. Data 9, 677 (2022).
20. Jennings, K. S., Winchell, T. S., Livneh, B. & Molotch, N. P. Spatial variation of the rain–snow temperature threshold across the Northern Hemisphere. Nat. Commun. 9, 1148 (2018).

21. Stone, L., Strong, C., Bai, H., Reichler, T., McCabe, G. & Brooks, P. D. Atlantic–Pacific influence on western U.S. hydroclimate and water resources. npj Clim. Atmos. Sci. 6, 139 (2023).
22. Held, I. M., Ting, M. & Wang, H. Northern winter stationary waves: theory and modeling. J. Clim. 15, 2125–2144 (2002).
23. Lorenz, D. J. & Hartmann, D. L. Eddy–zonal flow feedback in the Northern Hemisphere winter. J. Clim. 16, 1212–1227 (2003).
24. Scaife, A. A. & Smith, D. A signal-to-noise paradox in climate science. npj Clim. Atmos. Sci. 1, 28 (2018).
25. Weigel, A. P., Liniger, M. A. & Appenzeller, C. The discrete Brier and ranked probability skill scores. Mon. Weather Rev. 135, 118–124 (2007).
26. Knowles, N., Dettinger, M. D. & Cayan, D. R. Trends in snowfall versus rainfall in the western United States. J. Clim. 19, 4545–4559 (2006).
27. Klos, P. Z., Link, T. E. & Abatzoglou, J. T. Extent of the rain–snow transition zone in the western U.S. under historic and projected climate. Geophys. Res. Lett. 41, 4560–4568 (2014).
28. Enfield, D. B., Mestas-Nuñez, A. M. & Trimble, P. J. The Atlantic Multidecadal Oscillation and its relation to rainfall and river flows in the continental U.S. Geophys. Res. Lett. 28, 2077–2080 (2001).
29. McCabe, G. J., Palecki, M. A. & Betancourt, J. L. Pacific and Atlantic Ocean influences on multidecadal drought frequency in the United States. Proc. Natl. Acad. Sci. USA 101, 4136–4141 (2004).
30. Ruprich-Robert, Y. et al. Assessing the climate impacts of the observed Atlantic multidecadal variability using the GFDL CM2.1 and NCAR CESM1 global coupled models. J. Clim. 30, 2785–2810 (2017).
31. Bretherton, C. S., Widmann, M., Dymnikov, V. P., Wallace, J. M. & Bladé, I. The effective number of spatial degrees of freedom of a time-varying field. J. Clim. 12, 1990–2009 (1999).
32. Michaelsen, J. Cross-validation in statistical climate forecast models. J. Clim. Appl. Meteorol. 26, 1589–1600 (1987).
33. Rayner, N. A. et al. Global analyses of sea surface temperature, sea ice, and night marine air temperature since the late nineteenth century. J. Geophys. Res. 108, 4407 (2003).

34. Daly, C. et al. Physiographically sensitive mapping of climatological temperature and precipitation across the conterminous United States. Int. J. Climatol. 28, 2031–2064 (2008).
35. Fang, Y., Liu, Y. & Margulis, S. A. Western United States UCLA Daily Snow Reanalysis, Version 1 (WUS_UCLA_SR) [Data set]. NASA National Snow and Ice Data Center DAAC (2022).
36. Schneider, U., Becker, A., Finger, P., Rustemeier, E. & Ziese, M. GPCC Full Data Monthly Product Version 2020 at 1.0°: monthly land-surface precipitation from rain-gauges [Data set]. Global Precipitation Climatology Centre, DWD (2020).
37. Egger, G. & Reichler, T. Stratospheric winds shape winter precipitation in the American Southwest. Research Square preprint rs-10658139 (2026).
38. Bytheway, J. L. et al. Evaluation of wintertime precipitation estimates and forecasts in the mountains of Colorado. J. Hydrometeorol. 25, 565–579 (2024).
39. Rudisill, W. J. et al. Cold-season precipitation sensitivity to microphysical parameterizations: hydrologic evaluations leveraging snow lidar datasets. J. Hydrometeorol. 25, 143–160 (2024).
40. de Boer, G. et al. Supporting advancement in weather and water prediction in the Upper Colorado River Basin: the SPLASH campaign. Bull. Am. Meteorol. Soc. 104, E1853–E1874 (2023).
41. Lundquist, J. D. et al. Sublimation of snow. Bull. Am. Meteorol. Soc. 105, E975–E990 (2024).
42. Schwat, E. et al. Estimating snow sublimation in complex terrain: a season of intensive field measurements and the role of vertical water vapor flux divergence. J. Hydrometeorol. 26, 1455–1473 (2024).

Supplementary Files

This is a list of supplementary files associated with this preprint. Click to download.

- NPJSubmittedSupplementaryInformation.docx